Neoproterozoic hydrothermal activity in the West Australian Craton related to Rodinia assembly or breakup?

Hugo K.H. Olierook, Andrea Agangi, Diana Plavsa, Steven M. Reddy, Weihua Yao, Chris Clark, Sandra A. Occhipinti, Andrew R.C. Kylander-Clark

PII: S1342-937X(18)30296-X
DOI: https://doi.org/10.1016/j.gr.2018.10.019
Reference: GR 2057

To appear in: *Gondwana Research*

Received date: 22 May 2018
Revised date: 29 September 2018
Accepted date: 24 October 2018

Please cite this article as: Hugo K.H. Olierook, Andrea Agangi, Diana Plavsa, Steven M. Reddy, Weihua Yao, Chris Clark, Sandra A. Occhipinti, Andrew R.C. Kylander-Clark , Neoproterozoic hydrothermal activity in the West Australian Craton related to Rodinia assembly or breakup?. Gr (2018), https://doi.org/10.1016/j.gr.2018.10.019

Neoproterozoic hydrothermal activity in the West Australian Craton related to Rodinia assembly or breakup?

Hugo K. H. Olierook[1†]*, Andrea Agangi[1,2], Diana Plavsa[1,3], Steven M. Reddy[1], Weihua Yao[1,4], Chris Clark[1], Sandra A. Occhipinti[5], Andrew R. C. Kylander-Clark[6]

[1]School of Earth and Planetary Sciences, Curtin University, GPO Box U1987, Perth, WA 6845, Australia

[2]Department of Geology, University of Johannesburg, Auckland Park 2006, South Africa

[3]Future Industries Institute, University of South Australia, 101 Currie St, Adelaide, SA 5001, Australia

[4]Guangdong Provincial Key Lab of Geodynamics and Geohazards, School of Earth Sciences and Engineering, Sun Yat-sen University, Guangzhou 510275, China

[5]Centre for Exploration Targeting, School of Earth Sciences, University of Western Australia, 35 Stirling Highway, Crawley, WA 6009, Australia

[6]Earth Research Institute, University of California, Santa Barbara, CA 93106, USA

*Corresponding author: hugo.olierook@curtin.edu.au

Keywords: South China; rutile; U–Pb geochronology; Capricorn Orogen; Gascoyne

Abstract

The timing of final assembly and initiation of subsequent rifting of Rodinia is disputed. New rutile ages (913 ± 9 Ma, 900 ± 8 Ma and 873 ± 3 Ma) and published zircon, monazite, titanite, biotite, muscovite and xenotime geochronology from the Capricorn Orogen (West Australian Craton) reveal a significant early Neoproterozoic event characterized by very low to low metamorphic grade, abundant metasomatism, minor leucogranitic and pegmatitic magmatism and NW–SE fault reactivation episodes between ca. 955 and 830 Ma. Collectively, these are termed the ca. 955–830 Ma Kuparr Tectonic Event. An age range of ca. 955–830 Ma is concomitant with the final stages of Rodinia assembly and the initial stages of its attempted breakup. Very low- to low-grade metamorphic and structural geological evidence favour a distal north–south compressional regime as the driver for hydrothermal activity during ca. 955– 830 Ma. Nearby continental collision or accretion from the west (e.g., South China and/or Tarim) are ruled out. The cessation of metasomatism and magmatism in the West Australian Craton after ca. 830 Ma is concomitant with the emplacement of the Gairdner–Amata dyke swarm and associated magmatic activity in South China and Laurentia, the inception of the Adelaide Rift Complex and the deposition of the Centralian Superbasin. We posit that the cessation of hydrothermal activity in the Capricorn Orogen was caused by a tectonic switch from compressional to extensional at ca. 830 Ma. Magmatic and hydrothermal fluids were transferred away from the Capricorn Orogen to the incipient Adelaide Rift Complex, terminating metasomatism in the West Australian Craton.

1 INTRODUCTION

The assembly and breakup of ancient supercontinents are a focus of the Earth sciences. The configuration of supercontinents Pangea and Gondwana are relatively well established (Veevers, 2004) but more ancient supercontinents remain strongly debated. This is particularly the case with the Meso- to Neoproterozoic supercontinent Rodinia (Cawood et al., 2017; Li et al., 2008; Merdith et al., 2017; Wen et al., 2017). The true configuration during the final stages of its assembly remains elusive due to a paucity of magmatic rocks on which to obtain adequate paleomagnetic and geochronological constraints (Fig. 1). It follows that the onset of continental rifting is difficult to decipher because the basal ages of sedimentary basins cannot be reliably established. Moreover, extensional events are difficult to decode due to the overprinting of orogenic belts by Gondwanan and Pangean tectonism (e.g., the Pan–African Orogeny). The above problems mean that both the final assembly of Rodinia and its initiation of subsequent rifting are strongly debated. The final assembly is thought to have finished by ca. 850 Ma and initial extension is at least recorded by ca. 830 Ma but individual portions of Rodinia may have started to rift apart as early as ca. 1070 Ma (Camacho et al., 2015; Li et al., 2013; Tack et al., 2001). Having both collision and extension at the same time is geologically feasible, but the timing overlap makes it difficult to interpret these events on geochronological data alone. To better address the dynamics of supercontinent assembly and breakup, it thus becomes significant to understand when and where collisional/accretionary processes halted and subsequent extensional processes began to dominate.

Here, we present rutile geochronology and trace element geochemistry of nine samples from the Capricorn Orogen in the West Australian Craton, which reveal a series of hydrothermal events during ca. 915–870 Ma that has previously only been hinted at in Western Australia. Together with previously published ca. 955–830 Ma zircon, monazite, titanite, biotite, muscovite and xenotime geochronological data from the Capricorn Orogen, we evaluate the relationship and tectonic significance of this metasomatic activity, purported Rodinia configurations and the attempted breakup of the supercontinent. Ultimately, our data strengthens the argument that collisional and accretionary processes dominated until ca. 830 Ma, at which point extensional mechanisms began their attempted breakup of Rodinia.

2 GEOLOGICAL BACKGROUND OF THE CAPRICORN OROGEN

The Capricorn Orogen records a protracted tectonothermal history that amalgamated Archean–Paleoproterozoic terranes, welding the Pilbara Craton, Glenburgh Terrane and Yilgarn Craton to form the West Australian Craton (Fig. 2; Cawood and Tyler, 2004; Johnson et al., 2011b; Johnson et al., 2013). With over one billion years of intracontinental reworking and sedimentation spanning most of the Proterozoic, the complex tectonic history of the Capricorn Orogen is now subdivided into at least seven distinct tectonothermal events: (i) the 2215–2145 Ma Ophthalmia Orogeny, which sutured the Glenburgh Terrane to the Pilbara Craton (Krapež et al., 2017; Rasmussen et al., 2005), (ii) the 2005–1950 Ma Glenburgh Orogeny, which amalgamated the combined Pilbara Craton–Glenburgh Terrane with the Yilgarn Craton to form the West Australian Craton (Johnson et al., 2010; Johnson et al., 2011b; Occhipinti et al., 2004; Sheppard et al., 2004), (iii) the 1820–1770 Ma Capricorn

Orogeny, the first of a series of intracontinental reworking events (Sheppard et al., 2010a), (iv) the 1680–1620 Ma Mangaroon Orogeny (Sheppard et al., 2005), (v) the 1320–1170 Ma Mutherbukin Tectonic Event (Johnson et al., 2011a; Korhonen et al., 2017), (vi) the 1030–955 Ma Edmundian Orogeny (Martin and Thorne, 2004; Occhipinti, 2007; Occhipinti and Reddy, 2009; Sheppard et al., 2007), and (vii) the c. 570 Ma Mulka Tectonic Event (Sheppard et al., 2010b; Wingate and Giddings, 2000). Additionally, a poorly defined low-grade metamorphic event is purported to have occurred during the early Neoproterozoic (Johnson et al., 2009; Korhonen et al., 2017; Occhipinti, 2007; Occhipinti and Reddy, 2009; Piechocka et al., 2017; Piechocka et al., 2018; Sheppard et al., 2007; Wingate et al., 2011). However, the cause of these Neoproterozoic ages is still a matter of speculation because their significance is not systematically interpreted in unison.

3 METHODOLOGY

3.1 Sample selection and preparation

Rutile grains in a total of 24 samples were dated and geochemically characterized in a regional study of the Capricorn Orogen between 2014 and 2017 (Plavsa et al., 2018). In this study, four of the 24 rutile samples are presented because only these four samples yielded reliable Neoproterozoic ages, an age bracket that has previously been poorly reported in Western Australia. Five other samples in the Capricorn Orogen (184160, 184161, 152526, 144898, 168937; see locations Fig. 2) may have also experienced Neoproterozoic tectonothermal events. However, the high percentage of common Pb in all rutile analyses from these five other samples did not yield concordant ages nor statistically reliable discordia

intercepts. An explanation for why only these samples show Neoproterozoic ages are evaluated in the discussion. For a full compendium of all rutile samples analyzed from the 2014–2017 Capricorn Orogen campaign, including those not presented here, see Plavsa et al. (2018).

Heavy mineral separates and thin sections for the selected samples were obtained from the Geological Survey of Western Australia (GSWA). From the four rutile samples presented in this study, one heavy mineral separate (sample 187403) was hand-picked and mounted in epoxy resin. The other three samples (70747, 190607 and 190608) were cut and sent for thin section preparation. To ensure a highly polished surface necessary for electron backscatter diffraction (EBSD), all four samples were finished with a 0.06 μm colloidal silica suspension polish for 3–4 hours in a NaOH solution (pH = 10) on a Vibromat II polisher. Finally, all samples were carbon coated.

3.2 Rutile imaging

TiO_2 phases were imaged using backscatter electron (BSE) on a Tescan MIRA3 field emission gun scanning electron microscope (FEG-SEM) at the John de Laeter Centre, Curtin University, Perth. The operating conditions include an accelerating voltage of 20 kV, 12–27 nm spot size and 14–20 mm working distance. TiO_2 phases were identified by EBSD on the same instrument. Full analytical procedures and operating conditions used for rutile imaging are found in Plavsa et al. (2018).

3.3 In situ U–Th–Pb and trace element analysis

U–Th–Pb isotopic and trace element measurements were made using a laser ablation split stream (LASS) at the University of California, Santa Barbara and at Curtin University, Perth between 2014 and 2017. A brief overview of operating conditions is given here; for a detailed outline of the LASS instrumentation and techniques, see Kylander-Clark et al. (2013). The operating conditions included spot sizes of 23–35 μm, laser fluences of 3–5 J cm^{-2}, laser pulses of ~100 ns and repetition rates of 4–5 Hz. The total acquisition time was 75 seconds, including 40 seconds of background signal collection, 20 second sample ablation and 15–17 second washout period. The sample surface was cleaned by firing two laser shots prior to each analysis in order to remove surface contamination. The ablated material was carried by He gas and subsequently mixed with Ar prior to input into the plasma.

During both analytical sessions, the set-up for carrying out U–Pb isotopic measurements was kept the same in order to ensure consistency between the two laboratories. The U–Pb measurements were carried out on the multicollector (MC-ICP-MS) consisting of 12 Faraday cups equipped with 10^{11} ohm resistors and four ETP discrete-dynode ion counters. The ^{238}U and ^{232}Th were measured using the Faraday cups and the ^{206}Pb, ^{207}Pb, ^{208}Pb and ^{204}Pb + Hg were measured on the ion counters. Post-acquisition data processing including calculations of U–Pb isotopic ratios and their uncertainties were carried out using Iolite software (Paton et al., 2011). Precision on individual analyses can be variable and largely depends on the concentration of U, Pb and Th, with lower concentrations yielding predictably lower precision. Mass-bias and instrumental drift corrections were carried out using the common standard-sample-standard bracketing method, with typical run consisting of a suite of NIST glass, matrix-matched internal standards and multiple rutile reference materials at the beginning and end of the run, with internal standards (Rutile R10) analysed throughout the

run, typically after 9 analyses of unknown grains. Up to 120 unknowns were commonly analysed in one run and the entire suite of samples was analysed during continuous acquisition over three days. To monitor the accuracy of the LASS method, multiple rutile reference materials were analysed during the entire analytical session. The primary standard used for standard-sample bracketing is rutile R10 from Gjerstad, South Norway (Luvizotto et al., 2009). Reference standards treated as unknowns during the analytical session to test the accuracy of the method include Suguluk-4 from Trans-Hudson Orogen, Canada (Bracciali et al., 2013), PCA-S207 from East Lake Athabasca region, Canada (Bracciali et al., 2013), rutile from weakly retrogressed high pressure eclogite in the NW part of Gurskøy, Norway (9826J; Kylander-Clark, 2008), R13 and R19 (Luvizotto et al., 2009; Zack et al., 2011) and Windmill Hill Quartzite (WHQ; Clark et al., 2000; Taylor et al., 2012). The uncertainty is typically <2% for majority of the standards analyzed and demonstrates the validity of the adopted analytical method.

Trace element concentrations for the reference materials and samples were measured simultaneously on an Agilent 7700x quadrupole ICP-MS. NIST and BHVO glasses were used as a calibration reference materials for concentration determination and to correct for any instrumental drift, mass bias and elemental fractionation. Internal standardization was done stoichiometrically assuming 100% TiO_2 (i.e. 59.94% Ti). Rutile standard R10 was monitored within each run along with the other reference materials (R13, R19, PCA, SUG, 9826J and WHQ). Measured trace elements include ^{49}Ti (internal standard), ^{27}Al, ^{28}*Si*, ^{43}*Ca*, ^{51}V, ^{52}Cr, ^{55}Mn, ^{56}Fe, ^{59}*Co*, ^{60}Ni, ^{63}Cu, ^{90}Zr, ^{93}Nb, ^{95}Mo, ^{118}Sn, ^{121}Sb, ^{178}Hf, ^{181}Ta and ^{182}W (elements in *italics* were only measured at the Curtin University LASS lab). Post-acquisition data processing was carried out using Iolite software (Paton et al., 2011) along with

concentration calculations using normalized sensitivity equations of Longerich et al. (1996). The precision on individual analyses is dependent on the spot size (approximately 1.2% better on average for 35 μm spot size) and the concentration of analyte element in the sample. Typical precision on individual analyses obtained during the analytical session are >5% for elements <10 ppm, 3–5% for elements between 10 and 100 ppm and typically <3% for elements >100 ppm. Uncertainties on individual spot measurements are cited at 2σ level and include the internal uncertainties associated with counting statistics only. For the analyses performed at Curtin University, ^{202}Hg, ^{204}Pb, ^{206}Pb, ^{207}Pb, ^{208}Pb, ^{232}Th and ^{238}U were measured on the Agilent quadrupole, allowing for reliable calibration of the concentrations of these elements. The U and Pb concentrations for samples run at Santa Barbara are approximations only as they could not be robustly compared to known standards.

Results were filtered for reliability by concordance, common Pb and mineral inclusions. Analyses are considered concordant if they overlap with a ^{207}Pb/^{206}Pb vs. ^{238}U/^{206}Pb concordia curve (Spencer et al., 2016). Concordant dates and mildly discordant analyses (<10% discordance) tend to have ^{206}Pb/^{208}Pb ratios >10, whereas more strongly discordant dates have ^{206}Pb/^{208}Pb ratios <20. As rutile does not favor the incorporation of Th, any ^{208}Pb can be reasonably assumed to have been inherited as common Pb except in the rare instances where Th is above detection limit (Zack and Kooijman, 2017). A ^{206}Pb/^{208}Pb cut-off value of 10 corroborates with empirical constraints in rutile from Zack et al. (2011). Therefore, analyses with ^{206}Pb/^{208}Pb<10 were considered unreliable. Due to the high number of discordant analyses, common Pb corrections such as those presented in Zack et al. (2011) were not applied. For concordant analyses, common Pb as indicated by ^{208}Pb is below detection limit for >90% of analyses. Analyses where inclusions of silicate minerals (mostly

quartz) and/or zircon, apatite, monazite and ilmenite were observed under BSE were filtered out of the dataset. All ages are presented as $^{238}U/^{206}Pb$ ages and uncertainties reported in the text are quoted at 2σ.

Zr-in-rutile temperatures were calculated from the LASS data using the method of Tomkins et al. (2007) at pressures of 4 kbar. This pressure is consistent with the metamorphic pressures in assemblages where rutile is stable during the ca. 1210–1170 Ma stage of the Mutherbukin Tectonic Event (see discussion for link to the Mutherbukin Tectonic Event; Korhonen et al., 2015; Korhonen et al., 2017).

Full isotopic and trace elemental data set for the samples is given in supplementary Table A.

4 RESULTS

4.1 Sample descriptions and petrographic characterization

Sample 70747 is a metasiltstone unit from a shear zone within the 2005–1970 Ma Dalgaringa Supersuite at the southern margin of the Gascoyne Province (Fig. 2). The main assemblage consists of quartz (40–45%) and chlorite (55–60%), with trace garnet and accessory rutile and zircon. Microgranular quartz (0.5–1 mm) and chlorite define the foliation in the rock. Rutile forms euhedral to subhedral individual grains or fine-grained anhedral aggregates occasionally up to ~300–400 μm in size within the chlorite-rich domains. They are commonly twinned, brown in colour and can be up to ~300–500 μm in size. The long axes of rutile grains are parallel to the foliation, suggesting they formed contemporaneously with the main fabric-forming event. Under BSE, rutile is mostly homogeneous but some zonation is

occasionally present (Fig. 3a; supplementary Fig. A). Sub-micrometre oriented ilmenite needles occur in a majority of grains, while some of the grains are deformed as evidenced twin plane bending (Plavsa et al., 2018).

Sample 187403 is a quartzite from the Mumba Psammite unit of the 2240–2125 Ma Moogie Metamorphics and it is located within the Mutherbukin Zone (Fig. 2). The entire sample was crushed for mineral separation, thus a complete petrographic report is not available. Electron backscatter diffraction (EBSD) revealed that rutile was the only TiO_2 phase in the sample (Plavsa et al., 2018). The rutile textures and luminescence under BSE are quite variable. Most common are homogeneous moderately to highly bright grains (Fig. 3b). Homogeneous less bright rutile grains are also present (supplementary Fig. B) as well as oscillatory zoned rims around moderately bright to bright grains (supplementary Fig. B). Some rutile grains show oscillatory zoning with Fe-rich cores (approaching ilmenite compositions) and Fe-poor rims (Fig. 3c; supplementary Fig. B). Grains with patchy brightness are also found, where the brighter patches correspond to regions enriched in W and Nb (supplementary Fig. B).

Sample 190607 and 190608, collected adjacent to each other, are pelitic gneisses from the 1840–1810 Ma Leake Springs Metamorphics (Fig. 2). Both samples comprise quartz, cordierite, fibrolite (sillimanite), chlorite, green biotite, feldspar and accessory muscovite, rutile and zircon. Quartz is polygonal, and biotite is mostly randomly oriented and interstitial to other major components. Large (up to 1.5mm) elongate cordierite grains contain inclusions of biotite, quartz, rutile and zircon grains with typical pleochroic halos. Cordierite rims are commonly embayed and replaced fibrolite–chlorite intergrowths. Rutile occurs as elongate prismatic, euhedral grains up to 500 µm in size, and in some cases rimmed by ilmenite. In

BSE images, rutile has homogenous brightness, and no zoning was observed (Fig. 3d; supplementary Fig. C, D). The textural features (sharp boundaries, euhedral habit) and the absence of zoning suggest that rutile is in equilibrium with the coexisting minerals.

4.2 U–Pb Geochronology

Rutile in sample 70747 yielded concordant to strongly discordant ages (Fig. 4). Concordant ages span between ca. 1200 and 900 Ma, with a peak at ca. 920 Ma (Fig. 4, supplementary Fig. E).

Rutile grains from sample 187403 yielded a variety of textures and a large proportion of concordant analyses, with most textures yielding both concordant and discordant analyses (Fig. 4). Patchy and zoned rutile did not yield concordant ages because of high common Pb and domain mixing, respectively. Concordant analyses range in $^{238}U/^{206}Pb$ dates between ca. 1200 and 850 Ma, with the largest population towards the younger end at ca. 900–850 Ma (green analyses in Fig. 4). A small peak also exists at ca. 1100 Ma. An inverse relationship exists between concordant grain date and BSE brightness. Individual rutile grains do not yield different age populations, with the exception of two grains. However, discordant, oscillatory rims around concordant bright to moderately-bright cores are common (Fig. 3b).

Rutile from sample 190607 and 190608 yielded a majority of concordant to mildly discordant dates (<10% discordance) spanning in the range of ca. 1160–850 Ma, with peaks at ca. 1100 and 900 Ma (Fig. 4). Both samples yielded similar age spectra. Given that 190607 and 190608 were from the same sampling site, their similar age distributions are not surprising.

Five other samples yielded U–Pb age spectra that could also record ages between ca. 1200 and 850 Ma (supplementary Fig. F). None of these samples yield concordant dates nor are

discordia intercepts statistically-consistent with a single population. It is possible that a similar spread of dates between 1200 and 850 Ma is present in some or all of these samples. However, the incorporation of variable proportions of common-Pb in rutile inhibits further interpretation of the data.

4.3 Trace element geochemistry

All four samples are classified as metapelitic rocks as opposed to metabasic rocks when using a log(Cr/Nb) discriminator for rutile (Fig. 5) (Triebold et al., 2007; Zack et al., 2004). This confirms petrographic observations at the meso- and micro-scale.

All samples show remarkably consistent Zr concentrations, which translate to homogeneous Zr-in-rutile temperatures that are consistent irrespective of age (Fig. 6). Sample 70747, 190607 and 190608 have consistent Zr-in-rutile temperatures even for analyses that are strongly discordant (Fig. 7). Sample 70747 has a weighted mean Zr-in-rutile temperatures for all analyses of 532 ± 7 °C (MSWD = 0.20, p = 1; Fig. 7). Sample 190607 and 190608 have identical Zr-in-rutile temperatures of 580 ± 5 °C (MSWD = 0.60, p = 0.96) and 580 ± 3 °C (MSWD = 0.35, p = 1), respectively (Fig. 7). Sample 187403 shows similarly homogeneous Zr-in-rutile temperatures for concordant and mildly discordant (<10% discordance) analyses, whereby the concordant data yield a weighted mean of 648 ± 3 °C (MSWD = 0.35, p = 1). Strongly discordant analyses have significantly lower and heterogeneous Zr-in-rutile temperatures, which are predominantly from analyses on patchy rutile grains and those forming rims around brighter grains (Fig. 7).

In samples 70747, 190607 and 190608, rutile has a relatively low abundance of cations other than Ti. All samples contain less than 6% trace element, with the exception of a few analyses

with high Al that are presumably due to inclusions. For measured elements in these three samples (V, Fe, Nb, Ta, Cr, W and Al), there is no age-dependent chemical variation. This in in marked contrast to concordant analyses from sample 187403, which shows strong age-dependent chemical variation in Fe, Nb, Ta, W and Al but not V or Cr (Fig. 8). The relatively higher concentrations of Fe, Nb, Ta and W accounts for the higher luminescence of rutile grains in BSE images. Iron shows a ~2:3 wt % relationship with Nb (R^2 = 0.88; Fig. 8), corresponding to a ~1:1 atomic of Fe to Nb. There is also decoupling between Nb and Ta at high Nb concentrations (>6%) to markedly higher Ta concentrations.

5 DISCUSSION

5.1 Explanation of ~300–350 Myr spread of concordant rutile ages

All four samples show a significant spread of rutile U–Pb ages between ca. 1200 and 850 Ma that are probably not geologically reasonable with a ~300–350 Myr geological event. Petrographic, geochemical and geochronological data indicate that samples 70747, 190607, 190608 and the pre-900 Ma grains in sample 187403 formed in a distinct process to the post-900 Ma grains in sample 187403.

Petrographic observations from samples 70747, 190607 and 190608 show that rutile formed adjacent to phyllosilicates (biotite or chlorite, Fig. 3), suggesting rutile formation from the breakdown of these phases. Luvizotto and Zack (2009) have shown that rutile formation from biotite breakdown occurs during prograde metamorphism at medium-grade conditions in metapelitic rocks. The presence of garnet in sample 70747 further supports a medium-grade metamorphic event. Irrespective of age, the consistently low concentrations of cations other

than Ti in rutile from samples 70747, 190607 and 190608 supports the notion that rutile from these samples formed at the same time (Fig. 8). Within individual samples, the remarkably consistent and high Zr-in-rutile temperatures (550–650 °C; Figs. 7, 8) further supports the interpretation that all rutile grains crystallized under the same conditions. (Ewing et al., 2015; Kooijman et al., 2010)The simplest explanation for the homogeneous and relatively high Zr-in-rutile temperatures is that all rutile grains crystallized at or before ca. 1200 Ma (recorded by red analyses, Fig. 4) and that a subsequent event at ca. 920 Ma caused partial (grey analyses, Fig. 4) to complete (green analyses, Fig. 4) Pb-loss and age resetting. Given that the Zr-in-rutile temperatures recorded in the samples overlap with the Pb closure temperature to Pb in rutile at ~550–650° C (Ewing et al., 2015; Kooijman et al., 2010), the ca. 1200 Ma ages could record either a crystallization event at this time or a cooling event shortly after crystallization (red analyses in Fig. 4). As Zr is much more resistant to diffusion in rutile than Pb (Cherniak, 2000; Cherniak et al., 2007), Pb was able to (partially) diffuse out of the rutile lattice during a low-grade Neoproterozoic metamorphic or hydrothermal event, but Zr remained immobile except for strongly discordant grains. One final piece of evidence supports the notion that at least two events are responsible for the observed ~300–350 Myr spread of concordant dates, one at or prior to ca. 1200 Ma (red analyses, Fig. 4) and a second at ca. 900 Ma (green analyses, Fig. 4). The ‘concordant’ dates between ca. 1200 and 900 Ma (grey analyses, Fig. 4) are potentially subtly discordant. For sample 70747, it is possible to plot each of the concordant dates on statistically reliable discordia lines (Fig. 4). Although this is not possible to do with single discordia lines for samples 190607/190608 (and 187403), the data spread still presents a strongly linear trend. The above evidence indicates that a medium-grade metamorphic event at upper greenschist/lower amphibolite facies

conditions produced rutile from the breakdown of phyllosilicates at or prior to ca. 1200 Ma and was reset by a lower-grade metamorphic or hydrothermal event at ca. 900 Ma.

Geochemical and geochronological data paints a different picture for the genesis of ca. 870 Ma rutile in sample 187403. Sample 187403 shows a strong age-dependent enrichment in Nb, Ta, W and Fe but only for analyses with dates younger than 900 Ma (Fig. 8). The extremely high Nb–Ta–W–Fe concentrations in post-900 Ma rutile in sample 187403 are incompatible with the breakdown of phyllosilicates. The implication here is that sample 187403 neocrystallized post-900 Ma rutile in the presence of hydrothermal fluids rich in Nb, Ta, W and Fe. The culprit for the source of these fluids is probably the same as those recorded by a suite of ca. 900 Ma Be-Ta-Nb-bearing leucogranites and W-skarns in the Mutherbukin Zone (Johnson et al., 2009; Piechocka et al., 2017). Importantly, the leucogranites were dated by U–Pb monazite because zircon only yielded xenocrystic dates (Piechocka et al., 2017). Co-crystallization of both zircon and quartz with rutile are necessary to buffer Zr and Si, respectively, to obtain a robust Zr-in-rutile temperature (Tomkins et al., 2007). Without these phases, most Zr will enter rutile and yield Zr-in-rutile temperatures that may be 200 °C higher than the real crystallization temperatures (Cabral et al., 2015). Crystallization temperatures of ~450 °C (i.e., ~200°C lower than the 650 °C Zr-in-rutile temperatures) are compatible with pegmatite crystallization temperatures and probably a much more realistic estimate of the temperature conditions at ca. 900 Ma (Thomas et al., 2000). Although the Zr-in-rutile temperatures of the pre-900 and post-900 Ma rutile grains are conspicuously similar, we suspect this is fortuitous. Rather, we attribute the post-900 Ma rutile grains to a hydrothermal event unrelated to the earlier pre-900 Ma grains and also unrelated to samples 70747, 190607 and 190608.

We calculate the age of the hydrothermal event in each sample using their youngest analyses, within error, that are interpreted to have experienced complete Pb-loss (Fig. 4, 9). There is a natural break in analyses in each sample, interpreted as the division between partial and complete Pb-loss (Fig. 4). The calculated ages for samples 70747, 190607/190608 and 187403 are 913 ± 9 Ma (MSWD = 0.98, p = 0.42), 899 ± 8 Ma (MSWD = 1.08, p = 0.37) and 873 ± 3 Ma (MSWD = 1.06, p = 0.34), respectively (Fig. 9). These calculations highlight that, within uncertainty, there are at least two separate hydrothermal events recorded by rutile, one at ca. 910–900 Ma and the other at ca. 870 Ma.

5.2 Causes of ca. 1200–870 Ma metamorphic and hydrothermal events in the Capricorn Orogen

The above interpretation of the rutile age and geochemical data argues for several distinct rutile crystallization events: at or before ca. 1200 Ma, between 1200 and 920 Ma, at ca. 910–900 Ma, and at ca. 870 Ma. These are systematically discussed below.

The event at or before ca. 1200 Ma is probably the best characterized in the region and is known as the 1320–1170 Ma Mutherbukin Tectonic Event (Johnson et al., 2011a; Korhonen et al., 2015; Korhonen et al., 2017). Previous work in the region by Korhonen et al. (2017) revealed the 1320–1170 Ma Mutherbukin Tectonic Event occurred at two stages, from ca. 1320–1270 Ma and ca. 1210 to 1170 Ma. The latter experienced peak metamorphic temperatures of 550 °C to >650 °C, which corroborates with the consistent 550–650°C Zr-in-rutile temperatures obtained in the ca. 1200 rutile grains and the 1200–900 Ma rutile grains that experienced partial Pb-loss. The decreasing Zr-in-rutile temperatures from sample 187403 to 190607/190608 to 70747 is probably a reflection of increasing distance to the

highest-grade metamorphism in the centre of the Mutherbukin Zone (Figs. 2, 6). Therefore, the ca. 1210–1170 Ma stage of the Mutherbukin Tectonic Event can explain initial crystallization of the ca. 1200 Ma rutile grains.

The presence of one or more intervening events between the Mutherbukin Tectonic Event and the hydrothermal events at 910–900 Ma is possible on the basis of the difficulty in constructing statistically reliable discordia intercepts. The culprit for an intervening event could well be the 1030–955 Ma Edmundian Orogeny (Occhipinti and Reddy, 2009; Piechocka et al., 2017; Sheppard et al., 2007). Alternatively, an unknown event at ca. 1120–1080 Ma may also be implicated, for which there are a significant number of spots in all four samples.

Lead-loss events at ca. 910–900 Ma and ca. 870 Ma are not well constrained in the Capricorn Orogen. The Pb-loss events could be attributed to the final stages of the Edmundian Orogeny. Although traditionally the Edmundian Orogeny was bracketed between 1030 and 955 Ma, a younger pegmatite at ca. 940 Ma (Wingate et al., 2011) and a monzogranite at ca. 900 Ma (Piechocka et al., 2017) may also be implicated. The first phase of the Edmundian Orogeny comprises greenschist- to amphibolite-facies metamorphism, deformation, metasomatism and magmatism between ca. 1030 and 990 Ma (Sheppard et al., 2007). The second phase involves very low to low-grade metamorphism, magmatism, metasomatism and re-activation of NW–SE trending structures since ca. 955 Ma (Korhonen et al., 2017; Piechocka et al., 2017; Sheppard et al., 2007). On this basis, Piechocka et al. (2017) considered dividing the Edmundian Orogeny into an early, medium-grade metamorphic stage and a later, predominantly hydrothermal stage. Alternatively, the ca. 910–900 Ma and ca. 870 Ma events

are unrelated to the Edmundian Orogeny. In this scenario, the post-955Ma hydrothermal activity and emplacement of leucogranites and pegmatites are a product of distinct metasomatic events.

We support the division of the Edmundian Orogeny into two phases (Piechocka et al., 2017) but propose that the second phase is equivalent to the 'Kuparr Tectonic Event' of Cutten and Johnson (2018). The difference in ages between all these hydrothermal events may simply be the availability of fluids for different major structural discontinuities at different times. Several other geochronometers support this interpretation (Fig. 10). Monazite and xenotime geochronology of rare earth element-bearing pegmatites and Th-rich leucogranites yielded ages between ca. 955 and 900 Ma (Piechocka et al., 2017). $^{40}Ar/^{39}Ar$ dating of biotite and white mica along structural discontinuities across the entire Gascoyne Province yielded ages that were also in the range of 955–830 Ma (Occhipinti, 2007; Occhipinti and Reddy, 2009; Piechocka et al., 2018). Preliminary in situ U–Th–Pb monazite and xenotime ages from low-grade Edmund Group slates within the Ti Tree Syncline also yielded ca. 900–850 Ma ages (cf. Johnson et al., 2009). Recent orogen-scale titanite petrochronology also identified several sites where recrystallized titanite was reset by metasomatism at 955–830 Ma (Olierook et al., in review). Finally, recent K–Ar dating of clay mineral-bearing fault gouges in the Edmund Basin also yielded ages in this period (Cutten and Johnson, 2018). So, rather than a localized event only recorded by rutile, there is clearly a broader hydrothermal overprint that is recorded by seven different minerals (monazite, titanite, rutile, biotite, muscovite, xenotime and clay minerals) all along the Gascoyne Province. All these hydrothermal events are adjacent to lithospheric-scale or major NW–SE to ENE–WSW structural discontinuities that are inferred to have played a significant role in channelling fluids from the lower crust/mantle

to the upper crust (Fig. 2). Using the term proposed by Cutten and Johnson (2018), we attribute all these hydrothermal events to the 955–830 Ma Kuparr Tectonic Event but note that metasomatism probably occurred in several distinct stages associated with structural re-activation. On the basis of currently available geochronological data, the 955–830 Ma Kuparr Tectonic Event may be subdivided into four distinct episodes at ca. 955–940, 920–900, 880–865 and 830 Ma (Fig. 10). However, we note that there are relatively little published data, so these subdivisions may be obscured by the relatively few samples in this age range to date.

A question that is raised from the above considerations is why ca. 910–900 and 870 Ma rutile ages are only present from these four samples when an additional twenty rutile samples from the Capricorn Orogen did not identify such an age population. There are five key factors that distinguish the four samples from other samples. First, hydrothermal activity is concentrated around re-activated faults, shear zones and fractures. Samples distal from major faults did not experience any hydrothermal fluids necessary for the crystallization or Pb-loss of rutile grains. Second, Neoproterozoic rutile is found exclusively in psammitic to pelitic rocks. The breakdown of biotite or chlorite appears to have been a key factor for forming rutile during the Mutherbukin Tectonic Event prior to ca. 1200 Ma. Even sample 187403 – defined as a quartzite – probably previously contained phyllosilicates on the basis of the trace elements in rutile. Third, these four samples are located in the central Gascoyne Province. All samples collected in other psammitic or pelitic units further south, north or east failed to yield rutile with Neoproterozoic dates because the Mutherbukin Tectonic Event was restricted to the Paradise to Limejuice Zones of the Gascoyne Province and the western Edmund Basin (Fig. 2; Johnson et al., 2011a; Korhonen et al., 2017; Olierook et al., in review). Fourth, more than twenty additional samples (mostly granitoids) that were collected and analyzed in the

regional Capricorn Orogen study contained titanite as the main Ti-bearing phase as opposed to rutile because of a higher Ca content in these samples (Olierook et al., in review). Lastly, several samples that did yield rutile from metapelitic rocks in the central Gascoyne Province and western Edmund Basin failed to yield any concordant dates (supplementary Fig. F).

5.3 Implications for assembly or breakup of Rodinia

The question remains what the tectonic drivers were for the hydrothermal activity during the 955–830 Ma Kuparr Tectonic Event. This period is crucial in Earth history as it marks a time when Rodinia was at maximum packing but immediately prior to extensional episodes that led to eventual breakup of the supercontinent (Li et al., 2013; Lyu et al., 2017; Xu et al., 2016). Below, we explore the options for linking the Kuparr Tectonic Event to the final stages of assembly and the initial stages of rifting of Rodinia.

Previous investigations postulated that the post-955 Ma ages in the Capricorn Orogen were related to Edmundian Orogeny, despite noting a change from greenschist–amphibolite facies to very low/low metamorphic grade (Occhipinti and Reddy, 2009; Piechocka et al., 2017; Sheppard et al., 2007). If the switch to lower metamorphic grade between ca. 990 and 955 Ma represented cooling and exhumation following a collisional or compressional phase of the Edmundian Orogeny, it seems implausibly long for it to last until ca. 830 Ma. Therefore, we argue that the driving forces for the Kuparr Tectonic Event were probably distinct to that of the earlier, ca. 1030–990 Ma stage of the Edmundian Orogeny.

Given the very low to low metamorphic grade, it is unlikely that the Kuparr Tectonic Event is related to any continental collision or accretion directly adjacent to the West Australian Craton. Some models involve the collision of the Yangtze with the Cathaysia Blocks directly

adjacent to the West Australian Craton at ca. 870 Ma (Cawood et al., 2013; Cawood et al., 2017). Given its purported close proximity to the West Australian Craton, it is highly unlikely that the Yangtze–Cathaysia collision occurred next to the Capricorn Orogen. Similarly, the proposed collision of the Kalahari Craton with the West Australian Craton around this time also seem unlikely (Jacobs et al., 2008; Occhipinti and Reddy, 2009). If any continents were adjacent to the western margin of the West Australian Craton (in present-day coordinates), we argue that their amalgamation was completed during the Edmundian Orogeny or earlier.

Far-field effects from continental collision(s) occurring with the margin of northern Australia (e.g., Tarim; Tang et al., 2016), eastern Australia (e.g., South China; Li et al., 2008) or elsewhere are possible (Piechocka et al., 2018). In the West Australian Craton, metasomatic activity is present from the southern Pilbara Craton to the Gascoyne Province, right through to the northern Yilgarn Craton along structural discontinuities (Fig. 2; Rasmussen et al., 2007; Rasmussen et al., 2010). Piechocka et al. (2018) argues for a north–south compressional event that reactivated these structural discontinuities as these are most compatible with dextral strike-slip of NW-trending faults in the north and exhumation in the southern part of the Capricorn Orogen (Piechocka et al., 2018). Structural discontinuities in Proterozoic orogens around Australia may equally have been reactivated during the rifting and eventual breakup of Rodinia and now buried beneath Neoproterozoic and Phanerozoic sedimentary rocks (e.g., Maidment et al., 2007).

An extensional, rift-related origin of the Kuparr Tectonic Event is also plausible. There is limited evidence for extensional structures in the Mutherbukin Zone but that is not necessarily prohibitive to an extensional system, particularly if these are only far-field effects

to a broader rift-related structure (Maidment et al., 2007; Sheppard et al., 2007). Similar extensional events may also be recorded elsewhere in Australia, perhaps with the opening of the Adelaide Rift Complex and the onset of the first sedimentary succession of the Centralian Superbasin. At ca. 830 Ma, opening of the Adelaide Rift Complex (Preiss, 2000) and extensional-related magmatism of the ca. 830–825 Ma Amata–Gairdner Dyke Swarm occurred (Wingate et al., 1998). The onset of deposition in the Centralian Superbasin remains relatively poorly constrained. The oldest detrital zircons at ca. 1050 Ma (Heavitree Formation; Kositcin et al., 2014) and the underlying Central Desert Dolerite Suite (976 ± 3 Ma; Wyborn et al., 1998) provide a maximum depositional age of ca. 975 Ma for the Centralian Superbasin. More than 1 km above the Heavitree Formation, spilitic volcanic rocks at the top of the Bitter Springs Group post-date the negative $\delta^{13}C$ anomaly dated at ca. 810–790 Ma (Klaebe et al., 2017; Schmid, 2017), implying that the Heavitree Formation is older than ca. 790 Ma. Given the lack of major disconformities between the Heavitree Formation and spilitic volcanic rocks (Maidment et al., 2007), it is unlikely that continuous deposition could have lasted for more than ~30–50 Myr for a >1 km succession. Although still poorly constrained, deposition of the Centralian Superbasin could have commenced at ca. 830 Ma, at the end of the Kuparr Tectonic Event. Elsewhere, extensional-related magmatism was also occurring in South China and Laurentia – both potentially proximal to Australia – marking the onset of attempted Rodinia breakup (Li et al., 2008). Thus, the timing of the onset of Rodinia breakup recorded in Australia, South China and Laurentia at ca. 830 Ma may be intimately related to the end of the Kuparr Tectonic Event.

We postulate that the onset of attempted breakup of Rodinia at ca. 830 Ma caused the cessation of metasomatic activity at ca. 830 Ma in the West Australian Craton. Structural

geological and geochronological evidence favours a north–south compressional regime during ca. 955–830 Ma, which would have channelled hydrothermal fluids along structural discontinuities and metasomatized the associated rocks (Piechocka et al., 2018). The tectonic switch from a compressional to extensional regime at ca. 830 Ma transferred magmatic and hydrothermal fluids to the incipient rift (Adelaide Rift Complex), which ceased fault re-activation in the Capricorn Orogen and associated metasomatism.

6 CONCLUSIONS

Rutile ages from three sample locations in the Capricorn Orogen yielded ages of 913 ± 9 Ma, 900 ± 8 Ma and 873 ± 3 Ma. Petrographic and geochemical observations imply that these rutile grains formed as part of hydrothermal activity associated with very low to low grade metamorphic conditions. Together with additional geochronological constraints, positions adjacent to NW- to ENE-striking structural discontinuities and very low to low grade metamorphic conditions, we attribute these rutile ages to the 955–830 Ma Kuparr Tectonic Event. This time period is conspicuously important for Rodinia assembly and attempted breakup. We rule out a cause from nearby collisional tectonics, such as the collision between the Yangtze and Cathaysia blocks. Far-field collisional tectonics are the most plausible explanation for hydrothermal activity between 955 and 830 Ma in the Capricorn Orogen, although extension is an alternative. The cessation of hydrothermal activity is concomitant with the Amata–Gairdner Dyke Swarm and other associates in South China and Laurentia, as well as probably concomitant with the onset of deposition in the Adelaide Rift Complex and Centralian Superbasin. We propose that the onset of attempted breakup of Rodinia at ca. 830

Ma caused the cessation of metasomatic activity in the Capricorn Orogen, further constraining the early fragmentation of the supercontinent.

Acknowledgements

This research was funded by the Science and Industry Endowment Fund as part of The Distal Footprints of Giant Ore Systems: UNCOVER Australia Project (RP04-063) — Capricorn Distal Footprints. We thank Simon P. Johnson for comments on an early version of this manuscript.

References

Bracciali, L., Parrish, R.R., Horstwood, M.S.A., Condon, D.J., Najman, Y., 2013. UPb LA-(MC)-ICP-MS dating of rutile: New reference materials and applications to sedimentary provenance. Chemical Geology 347, 82-101.

Camacho, A., Armstrong, R., Davis, D.W., Bekker, A., 2015. Early history of the Amadeus Basin: Implications for the existence and geometry of the Centralian Superbasin. Precambrian Research 259, 232-242.

Cawood, P.A., Tyler, I.M., 2004. Assembling and reactivating the Proterozoic Capricorn Orogen: lithotectonic elements, orogenies, and significance. Precambrian Research 128, 201-218.

Cawood, P.A., Wang, Y., Xu, Y., Zhao, G., 2013. Locating South China in Rodinia and Gondwana: A fragment of greater India lithosphere? Geology 41, 903-906.

Cawood, P.A., Zhao, G., Yao, J., Wang, W., Xu, Y., Wang, Y., 2017. Reconstructing South China in Phanerozoic and Precambrian supercontinents. Earth-Science Reviews.

Chen, H., Chen, Y., Ripley, E.M., Li, C., Deng, X., Yue, S., Zheng, Z., Fu, B., 2017. Isotope and trace element studies of the Xingdi II mafic–ultramafic complex in the northern rim of the Tarim Craton: Evidence for emplacement in a Neoproterozoic subduction zone. Lithos 278, 274-284.

Cherniak, D.J., 2000. Pb diffusion in rutile. Contributions to Mineralogy and Petrology 139, 198-207.

Cherniak, D.J., Manchester, J., Watson, E.B., 2007. Zr and Hf diffusion in rutile. Earth and Planetary Science Letters 261, 267-279.

Clark, D.J., Hensen, B.J., Kinny, P.D., 2000. Geochronological constraints for a two-stage history of the Albany–Fraser Orogen, Western Australia. Precambrian Research 102, 155-183.

Cutten, H.N., Johnson, S.P., 2018. Kuparr Tectonic Event (KU): WA Geology Online, Explanatory Notes extract. Geological Survey of Western Australia, viewed 19th September, 2018 <www.dmp.wa.gov.au/ens>.

Ewing, T.A., Rubatto, D., Beltrando, M., Hermann, J., 2015. Constraints on the thermal evolution of the Adriatic margin during Jurassic continental break-up: U–Pb dating of rutile from the Ivrea–Verbano Zone, Italy. Contributions to Mineralogy and Petrology 169, 44.

Ge, R., Zhu, W., Wilde, S.A., He, J., Cui, X., Wang, X., Bihai, Z., 2014. Neoproterozoic to Paleozoic long-lived accretionary orogeny in the northern Tarim Craton. Tectonics 33, 302-329.

Jacobs, J., Pisarevsky, S., Thomas, R.J., Becker, T., 2008. The Kalahari Craton during the assembly and dispersal of Rodinia. Precambrian Research 160, 142-158.

Johnson, S., Sheppard, S., Thorne, A., Rasmussen, B., Fletcher, I., Wingate, M., Cutten, H., 2011a. The role of the 1280–1250 Ma Mutherbukin Tectonic Event in shaping the crustal architecture and mineralization history of the Capricorn Orogen. GSWA 2011 extended abstracts: promoting the prospectivity of Western Australia, 1-3.

Johnson, S.P., Sheppard, S., Rasmussen, B., Muhling, J.R., Fletcher, I.R., Wingate, M.T.D., Kirkland, C.L., Pirajno, F., 2009. Meso- to Neoproterozoic reworking in the Gascoyne Complex and what it means for mineral exploration. Geological Survey of Western Australia, p. 3p.

Johnson, S.P., Sheppard, S., Rasmussen, B., Wingate, M.T.D., Kirkland, C.L., Muhling, J.R., Fletcher, I.R., Belousova, E., 2010. The Glenburgh Orogeny as a record of Paleoproterozoic continent–continent collision. Geological Survey of Western Australia, Report 2010/5, 54p.

Johnson, S.P., Sheppard, S., Rasmussen, B., Wingate, M.T.D., Kirkland, C.L., Muhling, J.R., Fletcher, I.R., Belousova, E.A., 2011b. Two collisions, two sutures: Punctuated pre-1950 Ma assembly of the West Australian Craton during the Ophthalmian and Glenburgh Orogenies. Precambrian Research 189, 239-262.

Johnson, S.P., Thorne, A.M., Tyler, I.M., Korsch, R.J., Kennett, B.L.N., Cutten, H.N., Goodwin, J., Blay, O., Blewett, R.S., Joly, A., Dentith, M.C., Aitken, A.R.A., Holzschuh, J., Salmon, M., Reading, A., Heinson, G., Boren, G., Ross, J., Costelloe, R.D., Fomin, T., 2013. Crustal architecture of the Capricorn Orogen, Western Australia and associated metallogeny. Australian Journal of Earth Sciences 60, 681-705.

Klaebe, R.M., Kennedy, M.J., Jarrett, A.J.M., Brocks, J.J., 2017. Local paleoenvironmental controls on the carbon-isotope record defining the Bitter Springs Anomaly. Geobiology 15, 65-80.

Kooijman, E., Mezger, K., Berndt, J., 2010. Constraints on the U–Pb systematics of metamorphic rutile from in situ LA-ICP-MS analysis. Earth and Planetary Science Letters 293, 321-330.

Korhonen, F.J., Johnson, S.P., Fletcher, I.R., Rasmussen, B., Sheppard, S., Muhling, J.R., Dunkley, D.J., Wingate, M.T.D., Roberts, M.P., Kirkland, C.L., 2015. Pressure-temperature-time evolution of the Mutherbukin Tectonic Event, Capricorn Orogen. Geological Survey of Western Australia, Report 146, p. 70 p.

Korhonen, F.J., Johnson, S.P., Wingate, M.T.D., Kirkland, C.L., Fletcher, I.R., Dunkley, D.J., Roberts, M.P., Sheppard, S., Muhling, J.R., Rasmussen, B., 2017. Radiogenic heating and craton-margin plate stresses as drivers for intraplate orogeny. Journal of Metamorphic Geology 35, 631-661.

Kositcin, N., Whelan, J.A., Hallet, L., Beyer, E.E., 2014. Summary of results. Joint NTGS–GA geochronology project: Amadeus Basin, Arunta Region and Murphy Province, July 2012–June 2013. Northern Territory Geological Survey, Record 2014-005, p. 24.

Krapež, B., Müller, S.G., Fletcher, I.R., Rasmussen, B., 2017. A tale of two basins? Stratigraphy and detrital zircon provenance of the Palaeoproterozoic Turee Creek and Horseshoe basins of Western Australia. Precambrian Research 294, 67-90.

Kylander-Clark, A.R.C., 2008. Slow subduction and exhumation of a thick ultrahigh-pressure terrane: Western Gneiss Region, Norway. University of California, Santa Barbara, Ann Arbor, p. 121.

Kylander-Clark, A.R.C., Hacker, B.R., Cottle, J.M., 2013. Laser-ablation split-stream ICP petrochronology. Chemical Geology 345, 99-112.

Li, Z.-X., Bogdanova, S., Collins, A., Davidson, A., De Waele, B., Ernst, R., Fitzsimons, I., Fuck, R., Gladkochub, D., Jacobs, J., 2008. Assembly, configuration, and break-up history of Rodinia: a synthesis. Precambrian Research 160, 179-210.

Li, Z.-X., Evans, D.A.D., Halverson, G.P., 2013. Neoproterozoic glaciations in a revised global palaeogeography from the breakup of Rodinia to the assembly of Gondwanaland. Sedimentary Geology 294, 219-232.

Longerich, H.P., Jackson, S.E., Günther, D., 1996. Inter-laboratory note. Laser ablation inductively coupled plasma mass spectrometric transient signal data acquisition and analyte concentration calculation. Journal of Analytical Atomic Spectrometry 11, 899-904.

Luvizotto, G.L., Zack, T., 2009. Nb and Zr behavior in rutile during high-grade metamorphism and retrogression: An example from the Ivrea–Verbano Zone. Chemical Geology 261, 303-317.

Luvizotto, G.L., Zack, T., Meyer, H.P., Ludwig, T., Triebold, S., Kronz, A., Münker, C., Stockli, D.F., Prowatke, S., Klemme, S., Jacob, D.E., von Eynatten, H., 2009. Rutile crystals as potential trace element and isotope mineral standards for microanalysis. Chemical Geology 261, 346-369.

Lyu, P.-L., Li, W.-X., Wang, X.-C., Pang, C.-J., Cheng, J.-X., Li, X.-H., 2017. Initial breakup of supercontinent Rodinia as recorded by ca 860–840 Ma bimodal volcanism along the southeastern margin of the Yangtze Block, South China. Precambrian Research 296, 148-167.

Maidment, D.W., Williams, I.S., Hand, M., 2007. Testing long-term patterns of basin sedimentation by detrital zircon geochronology, Centralian Superbasin, Australia. Basin Research 19, 335-360.

Martin, D.M., Thorne, A.M., 2004. Tectonic setting and basin evolution of the Bangemall Supergroup in the northwestern Capricorn Orogen. Precambrian Research 128, 385-409.

Merdith, A.S., Collins, A.S., Williams, S.E., Pisarevsky, S., Foden, J.D., Archibald, D.B., Blades, M.L., Alessio, B.L., Armistead, S., Plavsa, D., Clark, C., Müller, R.D., 2017. A full-plate global reconstruction of the Neoproterozoic. Gondwana Research 50, 84-134.

Occhipinti, S.A., 2007. Neoproterozoic reworking in the Paleoproterozoic Capricorn Orogen: evidence from 40Ar/39Ar ages. Geological Survey of Western Australia Record 2007/10, pp. 1-41.

Occhipinti, S.A., Reddy, S.M., 2009. Neoproterozoic reworking of the Palaeoproterozoic Capricorn Orogen of Western Australia and implications for the amalgamation of Rodinia. Geological Society, London, Special Publications 327, 445-456.

Occhipinti, S.A., Sheppard, S., Passchier, C., Tyler, I.M., Nelson, D.R., 2004. Palaeoproterozoic crustal accretion and collision in the southern Capricorn Orogen: the Glenburgh Orogeny. Precambrian Research 128, 237-255.

Olierook, H.K.H., Taylor, R.J.M., Erickson, T.M., Clark, C., Reddy, S.M., Jahn, I., Kirkland, C.L., Barham, M., Wade, B.P., in review. Unravelling complex geologic histories using U–Pb and trace element systematics of titanite. Chemical Geology.

Paton, C., Hellstrom, J., Paul, B., Woodhead, J., Hergt, J., 2011. Iolite: Freeware for the visualisation and processing of mass spectrometric data. Journal of Analytical Atomic Spectrometry 26, 2508-2518.

Piechocka, A.M., Gregory, C.J., Zi, J.-W., Sheppard, S., Wingate, M.T.D., Rasmussen, B., 2017. Monazite trumps zircon: applying SHRIMP U–Pb geochronology to systematically evaluate emplacement ages of leucocratic, low-temperature granites in a complex Precambrian orogen. Contributions to Mineralogy and Petrology 172, 63.

Piechocka, A.M., Sheppard, S., Fitzsimons, I.C.W., Johnson, S.P., Rasmussen, B., Jourdan, F., 2018. Neoproterozoic $^{40}Ar/^{39}Ar$ mica ages mark the termination of a billion years of intraplate reworking in the Capricorn Orogen, Western Australia. Precambrian Research 310, 391-406.

Plavsa, D., Reddy, S., Clark, C., Agangi, A., 2018. Capricorn Orogen regional rutile study: a combined EBSD and Laser- Ablation Split-Stream (LASS) analytical approach. Geological Survey of Western Australia, Record 2018/15.

Preiss, W.V., 2000. The Adelaide Geosyncline of South Australia and its significance in Neoproterozoic continental reconstruction. Precambrian Research 100, 21-63.

Rasmussen, B., Fletcher, I.R., Muhling, J.R., Thorne, W.S., Broadbent, G.C., 2007. Prolonged history of episodic fluid flow in giant hematite ore bodies: Evidence from in situ U–Pb geochronology of hydrothermal xenotime. Earth and Planetary Science Letters 258, 249-259.

Rasmussen, B., Fletcher, I.R., Muhling, J.R., Wilde, S.A., 2010. In situ U–Th–Pb geochronology of monazite and xenotime from the Jack Hills belt: Implications for the age of deposition and metamorphism of Hadean zircons. Precambrian Research 180, 26-46.

Rasmussen, B., Fletcher, I.R., Sheppard, S., 2005. Isotopic dating of the migration of a low-grade metamorphic front during orogenesis. Geology 33, 773-776.

Schmid, S., 2017. Neoproterozoic evaporites and their role in carbon isotope chemostratigraphy (Amadeus Basin, Australia). Precambrian Research 290, 16-31.

Sheppard, S., Bodorkos, S., Johnson, S.P., Wingate, M.T.D., Kirkland, C.L., 2010a. The Paleoproterozoic Capricorn Orogeny: Intracontinental reworking not continent–continent collision. Geological Survey of Western Australia, Report 108, 33p.

Sheppard, S., Johnson, S.P., Wingate, M.T.D., Kirkland, C.L., Pirajno, F., 2010b. Explanatory notes for the Gascoyne Province. Geological Survey of Western Australia, Perth, Western Australia.

Sheppard, S., Occhipinti, S.A., Nelson, D.R., 2005. Intracontinental reworking in the Capricorn Orogen, Western Australia: the 1680–1620 Ma Mangaroon Orogeny. Australian Journal of Earth Sciences 52, 443-460.

Sheppard, S., Occhipinti, S.A., Tyler, I.M., 2004. A 2005–1970 Ma Andean-type batholith in the southern Gascoyne Complex, Western Australia. Precambrian Research 128, 257-277.

Sheppard, S., Rasmussen, B., Muhling, J.R., Farrell, T.R., Fletcher, I.R., 2007. Grenvillian-aged orogenesis in the Palaeoproterozoic Gascoyne Complex, Western Australia: 1030–950 Ma reworking of the Proterozoic Capricorn Orogen. Journal of Metamorphic Geology 25, 477-494.

Spencer, C.J., Kirkland, C.L., Taylor, R.J.M., 2016. Strategies towards statistically robust interpretations of in situ U–Pb zircon geochronology. Geoscience Frontiers 7, 581-589.

Tack, L., Wingate, M.T.D., Liégeois, J.P., Fernandez-Alonso, M., Deblond, A., 2001. Early Neoproterozoic magmatism (1000–910 Ma) of the Zadinian and Mayumbian Groups (Bas-Congo): onset of Rodinia rifting at the western edge of the Congo craton. Precambrian Research 110, 277-306.

Tang, Q., Zhang, Z., Li, C., Wang, Y., Ripley, E.M., 2016. Neoproterozoic subduction-related basaltic magmatism in the northern margin of the Tarim Craton: Implications for Rodinia reconstruction. Precambrian Research 286, 370-378.

Taylor, R., Clark, C., Reddy, S.M., 2012. The effect of grain orientation on secondary ion mass spectrometry (SIMS) analysis of rutile. Chemical Geology 300, 81-87.

Thomas, R., Webster, J.D., Heinrich, W., 2000. Melt inclusions in pegmatite quartz: complete miscibility between silicate melts and hydrous fluids at low pressure. Contributions to Mineralogy and Petrology 139, 394-401.

Tomkins, H.S., Powell, R., Ellis, D.J., 2007. The pressure dependence of the zirconium-in-rutile thermometer. Journal of Metamorphic Geology 25, 703-713.

Triebold, S., von Eynatten, H., Luvizotto, G.L., Zack, T., 2007. Deducing source rock lithology from detrital rutile geochemistry: An example from the Erzgebirge, Germany. Chemical Geology 244, 421-436.

Veevers, J.J., 2004. Gondwanaland from 650–500 Ma assembly through 320 Ma merger in Pangea to 185–100 Ma breakup: supercontinental tectonics via stratigraphy and radiometric dating. Earth-Science Reviews 68, 1-132.

Wen, B., Evans, D.A.D., Li, Y.-X., 2017. Neoproterozoic paleogeography of the Tarim Block: An extended or alternative "missing-link" model for Rodinia? Earth and Planetary Science Letters 458, 92-106.

Wingate, M.T.D., Campbell, I.H., Compston, W., Gibson, G.M., 1998. Ion microprobe U–Pb ages for Neoproterozoic basaltic magmatism in south-central Australia and implications for the breakup of Rodinia. Precambrian Research 87, 135-159.

Wingate, M.T.D., Giddings, J.W., 2000. Age and palaeomagnetism of the Mundine Well dyke swarm, Western Australia: implications for an Australia–Laurentia connection at 755 Ma. Precambrian Research 100, 335-357.

Wingate, M.T.D., Kirkland, C.L., Johnson, S.P., 2011. 190667: granite pegmatite, Camel Hill; Geochronology Record 1003. Geological Survey of Western Australia, pp. 1-6.

Wyborn, L., Hazell, M., Page, R., Idnurum, M., Sun, S.-S., 1998. A newly discovered major Proterozoic granite-alteration system in the Mount Webb region, central Australia, and implications for Cu-Au mineralization. AGSO Research Newsletter, 1-6.

Xu, X., Song, S., Allen, M.B., Ernst, R.E., Niu, Y., Su, L., 2016. An 850–820Ma LIP dismembered during breakup of the Rodinia supercontinent and destroyed by Early Paleozoic continental subduction in the northern Tibetan Plateau, NW China. Precambrian Research 282, 52-73.

Zack, T., Kooijman, E., 2017. Petrology and Geochronology of Rutile. Reviews in Mineralogy and Geochemistry 83, 443-467.

Zack, T., Stockli, D.F., Luvizotto, G.L., Barth, M.G., Belousova, E., Wolfe, M.R., Hinton, R.W., 2011. In situ U–Pb rutile dating by LA-ICP-MS: 208Pb correction and prospects for geological applications. Contributions to Mineralogy and Petrology 162, 515-530.

Zack, T., von Eynatten, H., Kronz, A., 2004. Rutile geochemistry and its potential use in quantitative provenance studies. Sedimentary Geology 171, 37-58.

Figure Captions

Fig. 1: Three examples of previously proposed Rodinia reconstructions at ca. 900 Ma that show different configurations of Australia (purple), South China/Tarim (yellow) and Greater India (blue). (a) Open ocean next to Western Australia with South China central to Rodinia in the missing-link model (Li et al., 2008). (b) South China and Greater India (Yangtze and Cathaysia Blocks) adjacent to Western Australia (Cawood et al., 2013; Cawood et al., 2017). Tarim is placed to the northwest of Australia (Chen et al., 2017; Ge et al., 2014; Tang et al., 2016). (c) Open ocean next to Western Australia with South China and Greater India separated from Rodinia (Merdith et al., 2017). The position of Tarim is uncertain in this configuration. Ant = Antarctica (Mawson); C = Cathaysia; Kal = Kalahari; Mad = Madagascar; Nth = North; Ra = Rayner; Y = Yangtze.

Fig. 2: Detailed geological map of the Capricorn Orogen, Western Australia, modified from Plavsa et al. (2018) annotated with geochronological data from this study and previous studies (Korhonen et al., 2017; Occhipinti and Reddy, 2009; Olierook et al., in review; Piechocka et al., 2017; Piechocka et al., 2018; Sheppard et al., 2007; this study; Wingate et al., 2011). musc. = muscovite

Fig. 3: Examples of most common textures in latest Mesoproterozoic to early Neoproterozoic rutile grains in backscatter electron (BSE) images (for a full catalogue of BSE images from

all analyzed rutile grains, see supplementary Figs. A–D). (a) Homogenous, moderately bright rutile surrounded by chlorite from sample 70747. (b) Homogeneous, moderately bright rutile from sample 187403. (c) Homogenous, moderately bright Neoproterozoic core with oscillatory zoned rim that contains a significant percentage of common Pb, from sample 187403. (d) Homogenous, moderately bright rutile adjacent to biotite and quartz.

Fig. 4: Tera–Wasserburg inverse concordia plots for four samples with some concordant rutile analyses (see supplementary Table A for data compilation). Key to ellipse color interpretations: colorless – discordant; red – original metamorphic rutile, grey – partial Pb-loss of original metamorphic rutile; green ellipses – complete Pb-loss or new metamorphic growth of rutile.

Fig. 5: Log (Cr/Nb) in rutile versus $^{238}U/^{206}Pb$ age for concordant rutile analyses, illustrating the exclusively pelitic affinity of analysed rutile. The Cr/Nb ratio discriminator for rutile is from Triebold et al. (2007).

Fig. 6: Zr-in-rutile temperatures versus $^{238}U/^{206}Pb$ age for concordant rutile analyses, illustrating that temperature is independent of age.

Fig. 7: Zr-in-rutile temperatures for all rutile analyses. Temperature is independent of degree of discordance for samples 70747, 190607 and 190608 and negligible for mildly discordant

analyses in sample 187403. However, strongly discordant analyses from sample 187403 have significantly lower Zr-in-rutile temperatures. Also note that 190607 and 190608 have statistically indistinguishable weighted mean Zr-in-rutile temperatures, compatible with them being sourced from the same locality. Zr-in-rutile temperatures were calculated using the method of Tomkins et al. (2007) using a pressure of 4 kbar.

Fig. 8: Trace element concentrations in rutile versus $^{238}U/^{206}Pb$ age for concordant rutile analyses. Note the inset in the Nb versus $^{238}U/^{206}Pb$ age panel highlights the ~2:3 wt% and ~1:1 atomic ratio of Fe to Nb.

Fig. 9: Weighted mean of $^{238}U/^{206}Pb$ dates interpreted to reflect complete Pb-loss or neocrystallised rutile during metasomatism. Sample 190607 and 190608 are grouped together because they were collected from the same sample site and therefore are interpreted to have experienced the same metasomatic history.

Fig. 10: Compilation of ages that are interpreted to belong to the Kuparr Tectonic Event (this study; Korhonen et al., 2017; Occhipinti and Reddy, 2009; Olierook et al., in review; Piechocka et al., 2017; Piechocka et al., 2018; Sheppard et al., 2007; Wingate et al., 2011). Note that mineral crystallization related to hydrothermal activity stops immediately before the purported onset of sedimentation in the Centralian Superbasin and Adelaide Rift

Complex, and before the emplacement of the Gairdner–Amata Dyke (G-A) dyke swarm. For full compilation of ages, see supplementary Table B.

Highlights

- Rutile in the Capricorn Orogen dated at 913 ± 9 Ma, 900 ± 8 Ma and 873 ± 3 Ma
- New Neoproterozoic series of tectonothermal events at ca. 955–830 Ma: Kuparr Event
- Metamorphic and structural geology favours distal N–S compressional drivers for metasomatism
- Continent collision of South China or Tarim to West Australian Craton ruled out
- Cessation of tectonothermal activity at ca. 830 Ma caused by attempted breakup of Rodinia

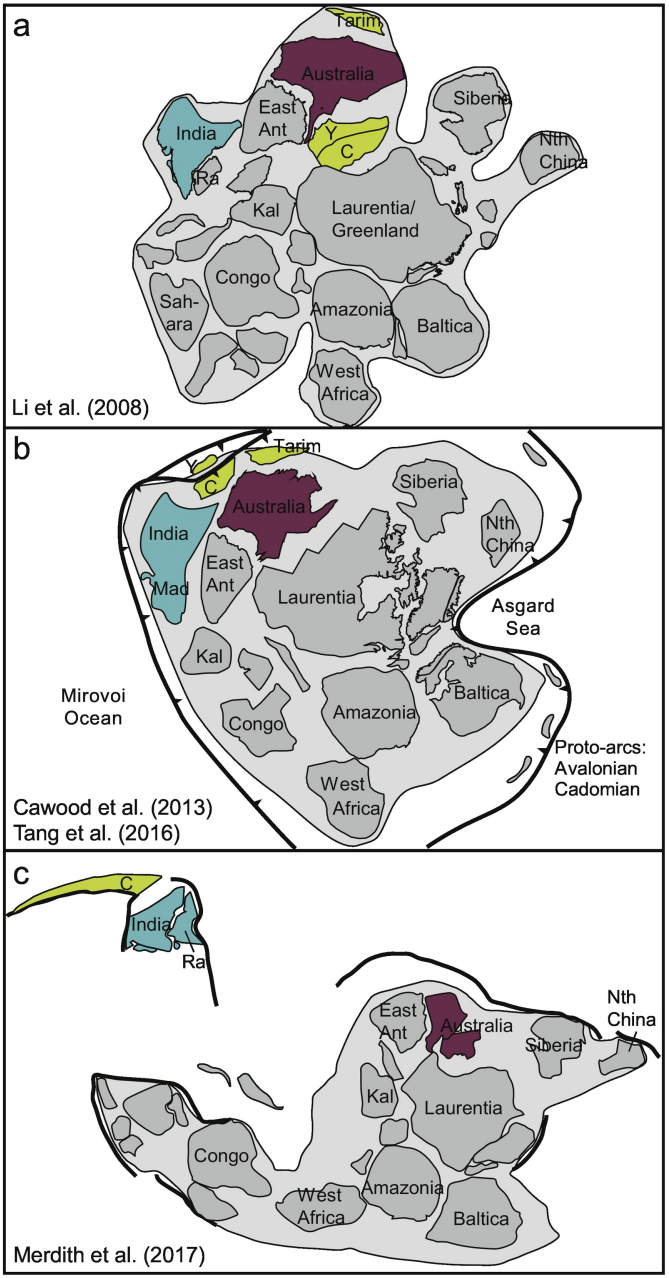
a
Tarim
Australia
East Ant
Siberia
India
Y
C
Nth China
Ra
Kal
Laurentia/ Greenland
Congo
Sah-ara
Amazonia
Baltica
West Africa
Li et al. (2008)
b
Tarim
Y
C
Siberia
Australia
India
Nth China
East Ant
Mad
Laurentia
Asgard Sea
Kal
Mirovoi Ocean
Amazonia
Baltica
Congo
Proto-arcs: Avalonian Cadomian
West Africa
Cawood et al. (2013)
Tang et al. (2016)
c
C
India
Ra
East Ant
Australia
Nth China
Siberia
Kal
Laurentia
Congo
Amazonia
West Africa
Baltica
Merdith et al. (2017)

Figure 1

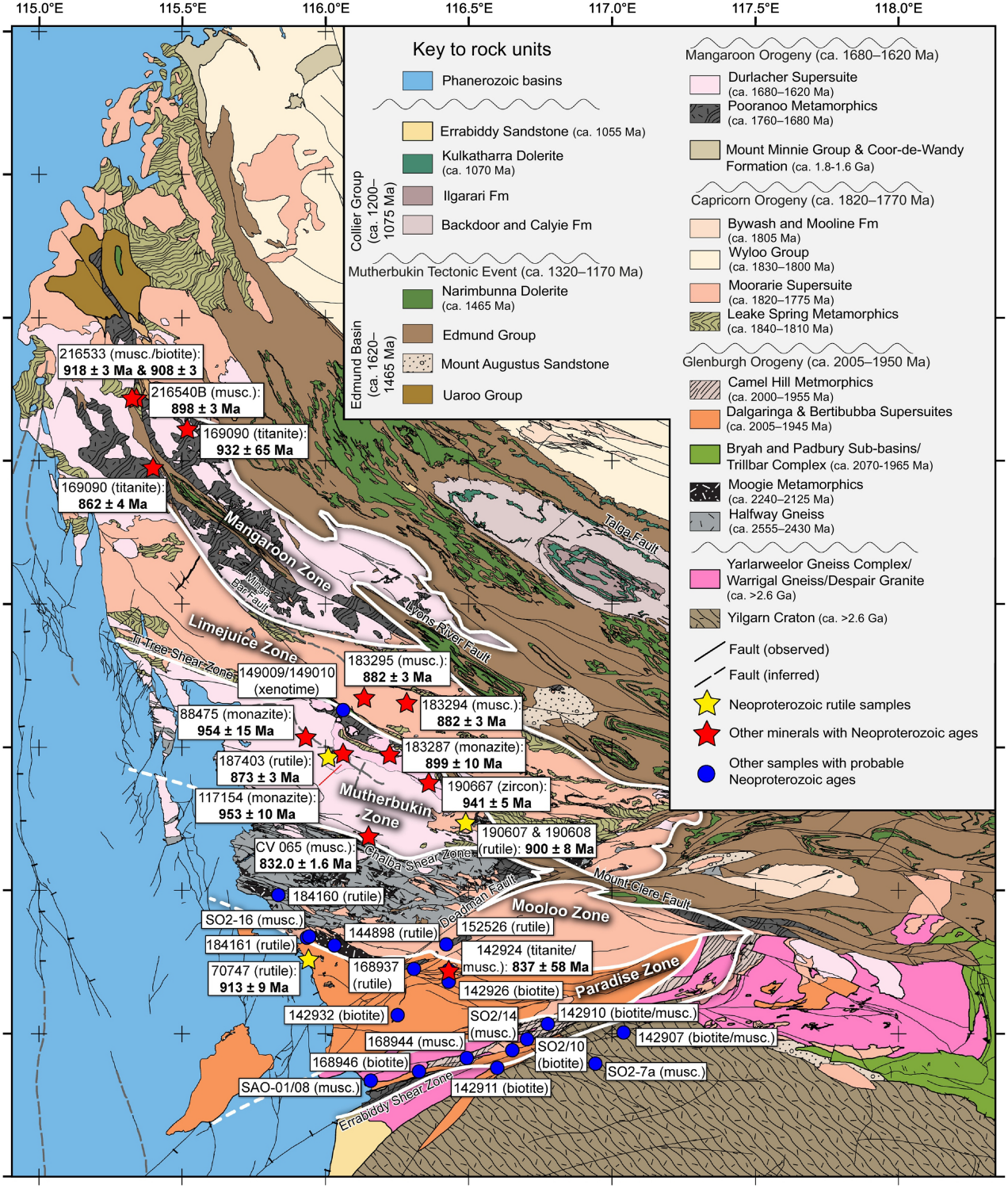
115.0°E
115.5°E
116.0°E
116.5°E
117.0°E
117.5°E
118.0°E
22.0°S
22.5°S
23.0°S
23.5°S
24.0°S
24.5°S
25.0°S
25.5°S
26.0°S
Key to rock units
Phanerozoic basins
Errabiddy Sandstone (ca. 1055 Ma)
Kulkatharra Dolerite (ca. 1070 Ma)
Ilgarari Fm
Backdoor and Calyie Fm
Collier Group (ca. 1200–1075 Ma)
Mutherbukin Tectonic Event (ca. 1320–1170 Ma)
Narimbunna Dolerite (ca. 1465 Ma)
Edmund Group
Mount Augustus Sandstone
Uaroo Group
Edmund Basin (ca. 1620–1465 Ma)
Mangaroon Orogeny (ca. 1680–1620 Ma)
Durlacher Supersuite (ca. 1680–1620 Ma)
Pooranoo Metamorphics (ca. 1760–1680 Ma)
Mount Minnie Group & Coor-de-Wandy Formation (ca. 1.8-1.6 Ga)
Capricorn Orogeny (ca. 1820–1770 Ma)
Bywash and Mooline Fm (ca. 1805 Ma)
Wyloo Group (ca. 1830–1800 Ma)
Moorarie Supersuite (ca. 1820–1775 Ma)
Leake Spring Metamorphics (ca. 1840–1810 Ma)
Glenburgh Orogeny (ca. 2005–1950 Ma)
Camel Hill Metmorphics (ca. 2000–1955 Ma)
Dalgaringa & Bertibubba Supersuites (ca. 2005–1945 Ma)
Bryah and Padbury Sub-basins/ Trillbar Complex (ca. 2070-1965 Ma)
Moogie Metamorphics (ca. 2240–2125 Ma)
Halfway Gneiss (ca. 2555–2430 Ma)
Yarlarweelor Gneiss Complex/ Warrigal Gneiss/Despair Granite (ca. >2.6 Ga)
Yilgarn Craton (ca. >2.6 Ga)
Fault (observed)
Fault (inferred)
Neoproterozoic rutile samples
Other minerals with Neoproterozoic ages
Other samples with probable Neoproterozoic ages
216533 (musc./biotite): 918 ± 3 Ma & 908 ± 3
216540B (musc.): 898 ± 3 Ma
169090 (titanite): 932 ± 65 Ma
169090 (titanite): 862 ± 4 Ma
Mangaroon Zone
Minga Bar Fault
Talga Fault
Lyons River Fault
Limejuice Zone
Ti-Tree Shear Zone
149009/149010 (xenotime)
183295 (musc.): 882 ± 3 Ma
183294 (musc.): 882 ± 3 Ma
88475 (monazite): 954 ± 15 Ma
187403 (rutile): 873 ± 3 Ma
183287 (monazite): 899 ± 10 Ma
190667 (zircon): 941 ± 5 Ma
117154 (monazite): 953 ± 10 Ma
Mutherbukin Zone
190607 & 190608 (rutile): 900 ± 8 Ma
CV 065 (musc.): 832.0 ± 1.6 Ma
Chalba Shear Zone
Deadman Fault
Mount Clere Fault
184160 (rutile)
SO2-16 (musc.)
144898 (rutile)
152526 (rutile)
Mooloo Zone
184161 (rutile)
142924 (titanite/ musc.): 837 ± 58 Ma
70747 (rutile): 913 ± 9 Ma
168937 (rutile)
142926 (biotite)
Paradise Zone
142932 (biotite)
SO2/14 (musc.)
142910 (biotite/musc.)
168944 (musc.)
142907 (biotite/musc.)
SO2/10 (biotite)
168946 (biotite)
SO2-7a (musc.)
SAO-01/08 (musc.)
142911 (biotite)
Errabiddy Shear Zone

Figure 2

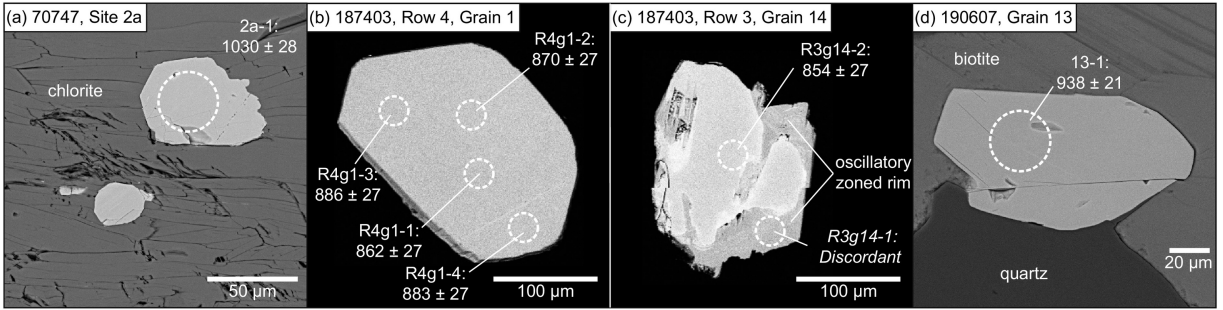
(a) 70747, Site 2a
2a-1:
1030 ± 28
chlorite
50 µm
(b) 187403, Row 4, Grain 1
R4g1-2:
870 ± 27
R4g1-3:
886 ± 27
R4g1-1:
862 ± 27
R4g1-4:
883 ± 27
100 µm
(c) 187403, Row 3, Grain 14
R3g14-2:
854 ± 27
oscillatory
zoned rim
R3g14-1:
Discordant
100 µm
(d) 190607, Grain 13
biotite
13-1:
938 ± 21
quartz
20 µm

Figure 3

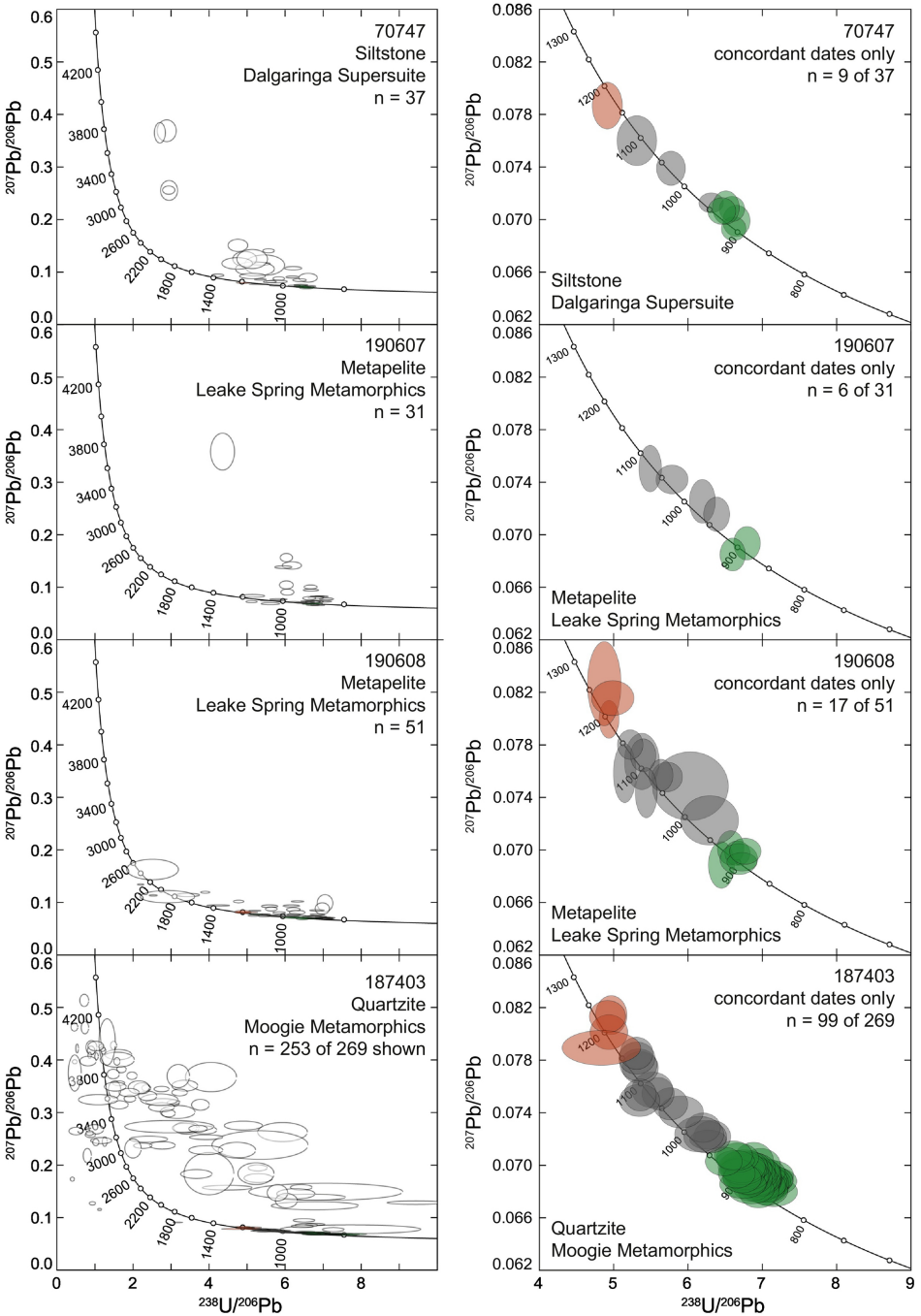
70747
Siltstone
Dalgaringa Supersuite
n = 37
70747
concordant dates only
n = 9 of 37
Siltstone
Dalgaringa Supersuite
190607
Metapelite
Leake Spring Metamorphics
n = 31
190607
concordant dates only
n = 6 of 31
Metapelite
Leake Spring Metamorphics
190608
Metapelite
Leake Spring Metamorphics
n = 51
190608
concordant dates only
n = 17 of 51
Metapelite
Leake Spring Metamorphics
187403
Quartzite
Moogie Metamorphics
n = 253 of 269 shown
187403
concordant dates only
n = 99 of 269
Quartzite
Moogie Metamorphics
207Pb/206Pb
238U/206Pb

Figure 4

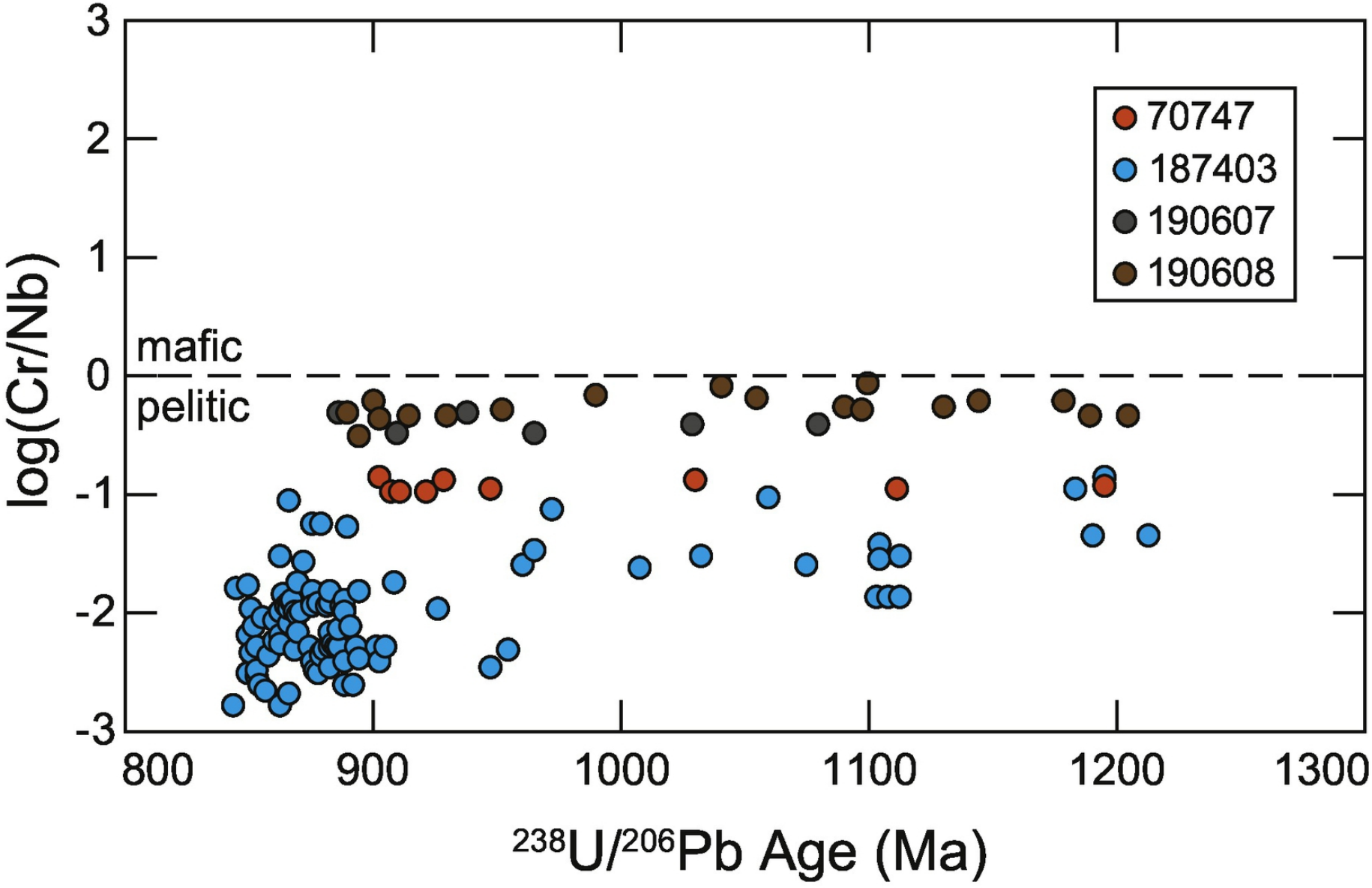
70747
187403
190607
190608
mafic
pelitic
log(Cr/Nb)
3
2
1
0
-1
-2
-3
800
900
1000
1100
1200
1300
238U/206Pb Age (Ma)

Figure 5

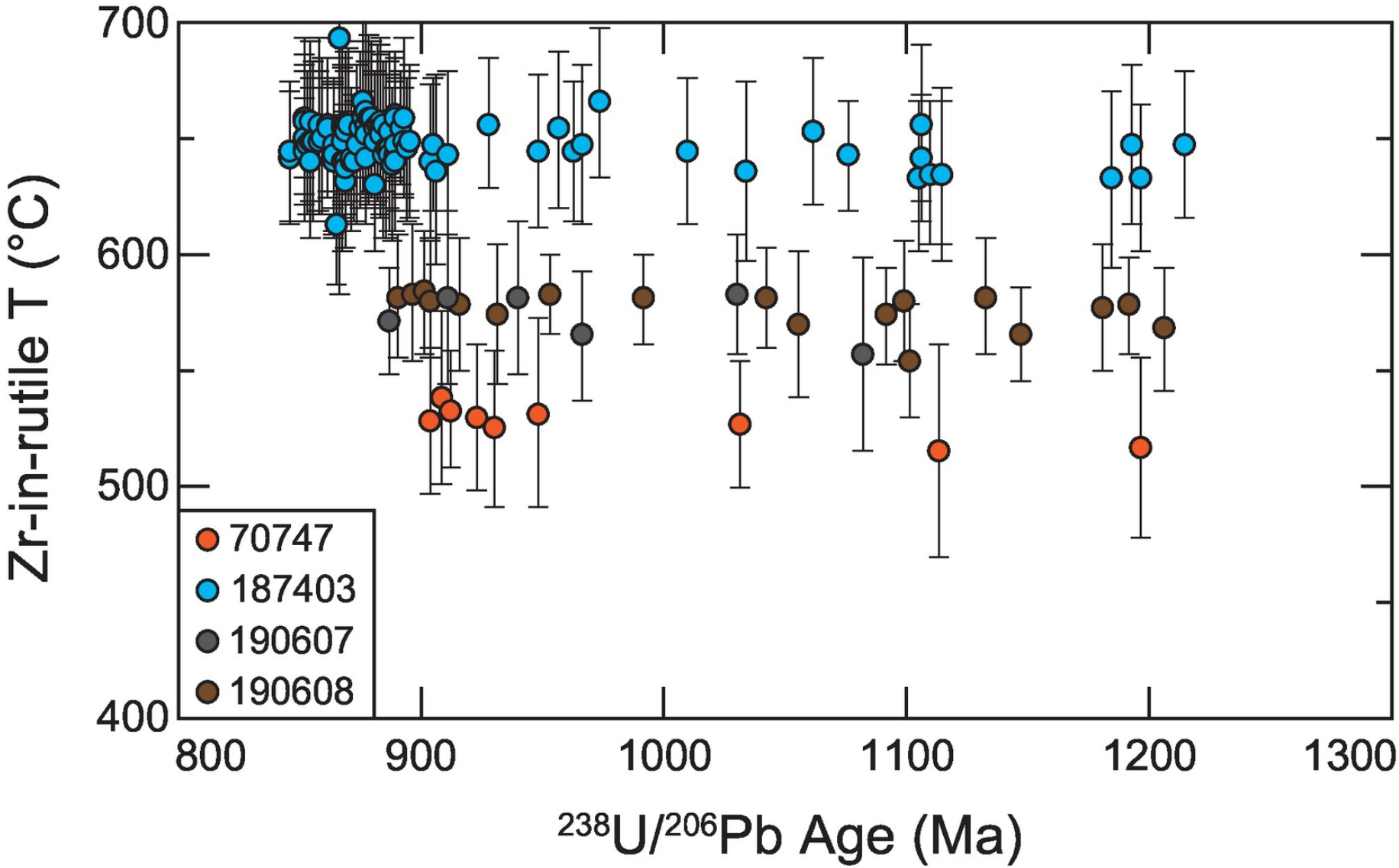
700
600
500
400
800
900
1000
1100
1200
1300
Zr-in-rutile T (°C)
238U/206Pb Age (Ma)
70747
187403
190607
190608

Figure 6

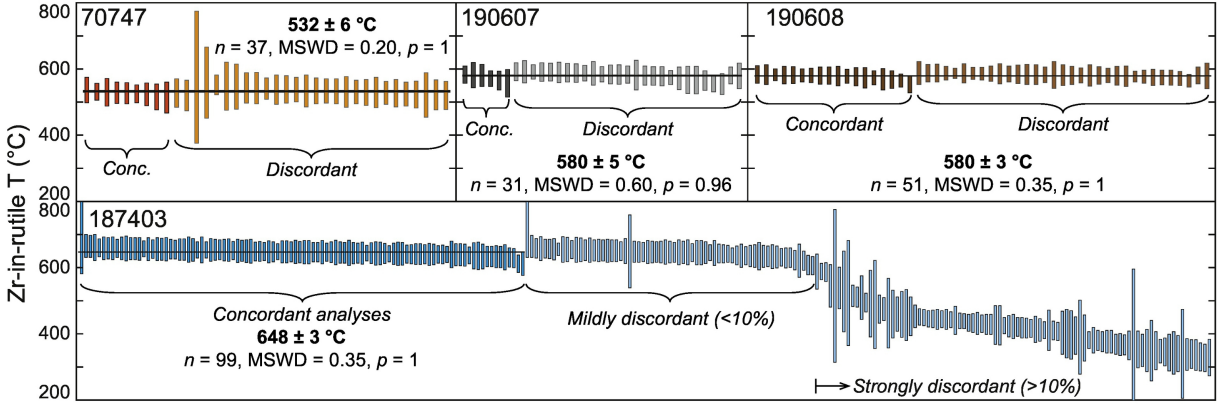
70747
532 ± 6 °C
n = 37, MSWD = 0.20, p = 1
Conc.
Discordant
190607
Conc.
Discordant
580 ± 5 °C
n = 31, MSWD = 0.60, p = 0.96
190608
Concordant
Discordant
580 ± 3 °C
n = 51, MSWD = 0.35, p = 1
187403
Concordant analyses
648 ± 3 °C
n = 99, MSWD = 0.35, p = 1
Mildly discordant (<10%)
Strongly discordant (>10%)
Zr-in-rutile T (°C)
800
600
400
200

Figure 7

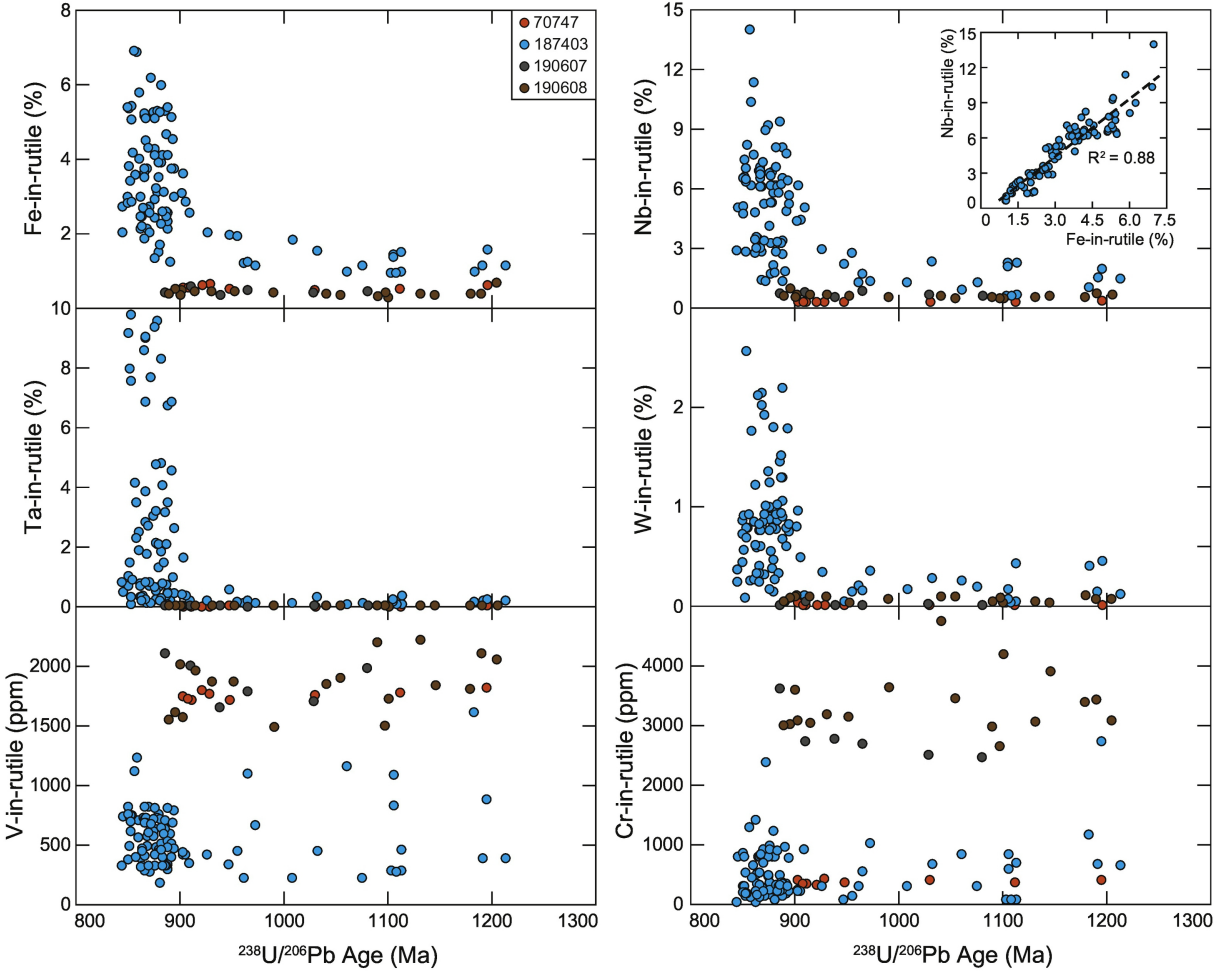
70747
187403
190607
190608
Fe-in-rutile (%)
Ta-in-rutile (%)
V-in-rutile (ppm)
Nb-in-rutile (%)
W-in-rutile (%)
Cr-in-rutile (ppm)
Nb-in-rutile (%)
Fe-in-rutile (%)
R² = 0.88
238U/206Pb Age (Ma)
238U/206Pb Age (Ma)

Figure 8

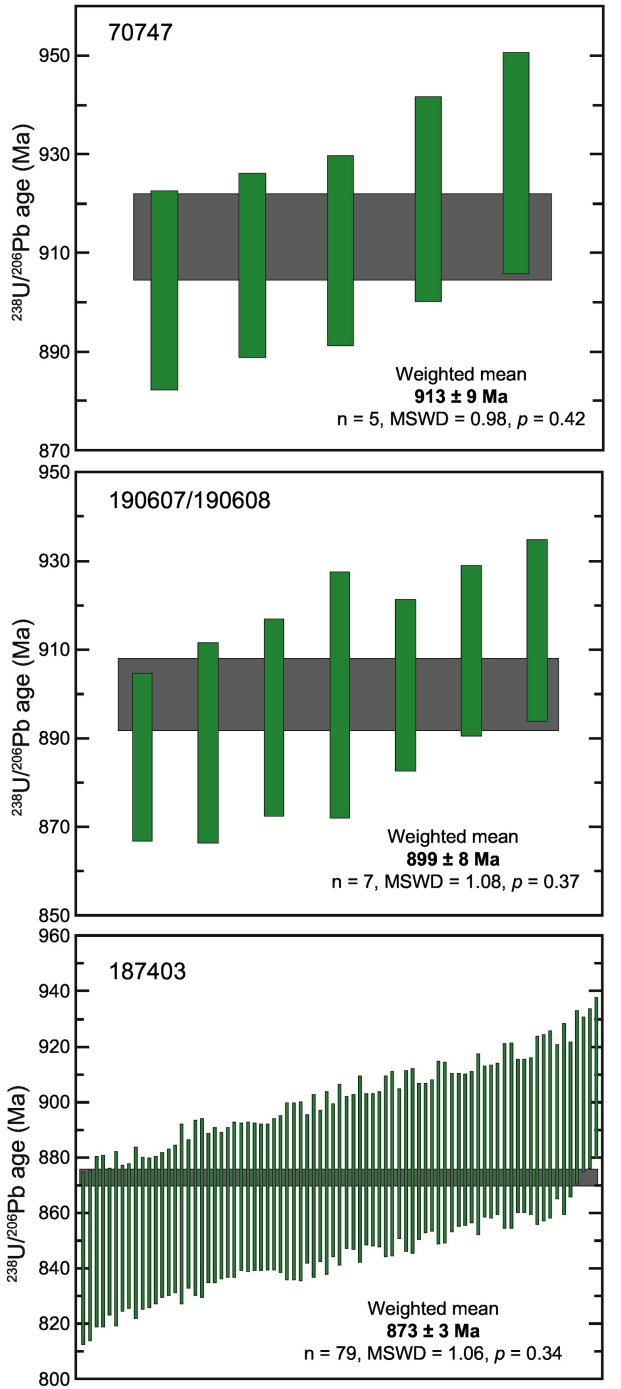
70747
950
930
910
890
870
$^{238}U/^{206}Pb$ age (Ma)
Weighted mean
913 ± 9 Ma
n = 5, MSWD = 0.98, *p* = 0.42
190607/190608
950
930
910
890
870
850
$^{238}U/^{206}Pb$ age (Ma)
Weighted mean
899 ± 8 Ma
n = 7, MSWD = 1.08, *p* = 0.37
187403
960
940
920
900
880
860
840
820
800
$^{238}U/^{206}Pb$ age (Ma)
Weighted mean
873 ± 3 Ma
n = 79, MSWD = 1.06, *p* = 0.34

Figure 9

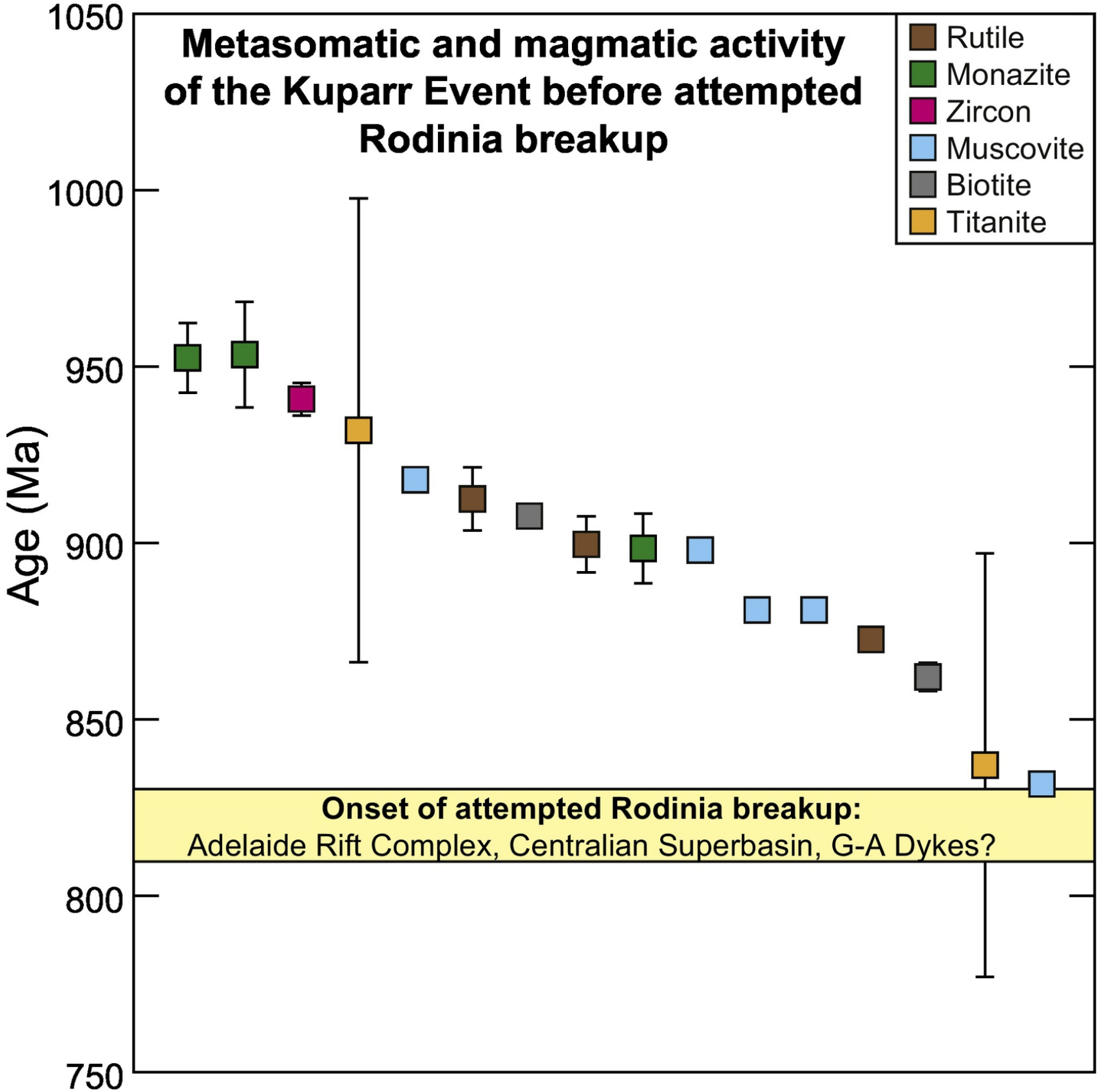
Metasomatic and magmatic activity of the Kuparr Event before attempted Rodinia breakup
Rutile
Monazite
Zircon
Muscovite
Biotite
Titanite
Age (Ma)
1050
1000
950
900
850
800
750
Onset of attempted Rodinia breakup:
Adelaide Rift Complex, Centralian Superbasin, G-A Dykes?

Figure 10